Study of recrystallization and activation processes in thin and highly doped silicon-on-insulator layers by nanosecond laser thermal annealing

Nicolas Chery, Meiling Zhang, Nicolas Mallet, Grégory Seine, Vincent Paillard, Jean-Marie Poumirol, Guilhem Larrieu, Richard Monflier, Anne-Sophie Royet, Sébastien Kerdilès, et al.

Study of recrystallization and activation processes in thin and highly doped SOI layers by nanosecond Laser Thermal Annealing

N. Chery,[1] M. Zhang,[1] R. Monflier,[2] N. Mallet,[2] G. Seine,[1] V. Paillard,[1] J. M. Poumirol,[1] G. Larrieu,[3] A.S. Royet,[4] S. Kerdiles,[4] P. Acosta-Alba,[4] M. Perego,[5] Caroline Bonafos,[1] and F. Cristiano[3]

[1)] *CEMES, CNRS and Université de Toulouse, 29 rue Jeanne Marvig, 31055 Toulouse, France*

[2)] *LAAS, CNRS and Université de Toulouse, 7 avenue du Colonel Roche, 31400 Toulouse, France*

[3)] *LAAS, CNRS and Université de Toulouse, 7 av. du Colonel Roche, 31400 Toulouse, France*

[4)] *Université Grenoble-Alpes, CEA-LETI, 17 avenue des Martyrs, 38054 Grenoble*

[5)] *MM-CNR, Unit of Agrate Brianza, Via C. Olivetti 2, I-20864 Agrate Brianza, Italy*

(*Electronic mail: fuccio.cristiano@laas.fr)

(*Electronic mail: caroline.bonafos@cemes.fr)

(*Electronic mail: nicolas.chery@cemes.fr)

(Dated: 5 October 2021)

Out-of-equilibrium thermal annealing processes such as melt laser thermal annealing are appealing as allowing strong local dopant activation well beyond the solid-state values. In this work, a thorough study of the phosphorus heavy doping of thin SOI layers involving UV nanosecond LTA is presented. The melting regimes and regrowth processes as well as the redistribution and activation of P in the top Si amorphized layer were studied as a function of the doping level and LTA conditions. The results highlight the crucial role of the thin crystalline Si layer preserved after amorphization of the top Si layer, which provides nucleation seeds for the liquid phase recrystallization. The doping concentration modifies the recrystallization processes by lowering the melt thresholds or reducing of the nucleation rate of crystal seeds, leading to unexpected amorphous layers after full melt. It also strongly influences the surface roughness, with the formation of crystalline hillocks at the surface at the onset of the full melt for the lowest P doses and flat surfaces for the highest ones. Phosphorus remains homogeneously distributed inside the SOI, reaching values exceeding the solid solubility limit of P in bulk Si at thermal equilibrium, despite pile-up at the native oxide resulting from the liquid phase epitaxy. Monocrystalline defect free layers with active dopant concentration close to the highest active values in bulk Si, with comparable mobilities, are obtained in optimised laser annealing conditions after the second melt regime, highlighting the great potential of UV nanosecond LTA for efficiently doping thin SOI layers.

I. INTRODUCTION

The general evolution of technologies in microelectronics has been marked for several decades by the ceaseless miniaturization of its basic component, the MOS transistor, in order to obtain greater circuit complexity, better performances and reduced costs. Historically, the production of doped source/drain zones has required a continuous reduction in their size, accompanied by an increase in the concentration of active dopants. In the context of new MOS architectures as FD-SOI or FinFET components which demonstrate increased activation and speed, reduced parasitic capacitance, and lower power consumption in Silicon-On-Insulator (SOI) substrates, fast anneal techniques have been explored to mitigate scaling issues. In particular, increased activation, especially for contact engineering, is now the highest priority. For this, out-of-equilibrium thermal annealing processes, such as laser thermal annealing (LTA), are studied to replace conventional thermal annealing. In addition to allowing the production of ultra-thin and ultra-doped junctions, LTA annealing is able to achieve very strong local activation (on the surface and in depth)[1] and a uniform distribution of dopants[2]. This process, studied in the research community since the 1980's for the manufacture of solar cells[3], or for more fundamental studies as the deep understanding of the laser annealing of damage in ion-implanted Si[4] (see also[5] and references therein), also offers new technological possibilities for the development of 3D architectures[6]. Indeed, in the case of nanosecond laser annealing, the short pulse duration as well as the short absorption length insures that only the surface of the material is heated, which is particularly appropriated to 3D sequential integration.

Highly doped thin Si layers are also appealing for new applications, out of the microelectronics field, as Infra-Red (IR) plasmonics. Surface Plasmon Polaritons (SPP) have been demonstrated on p and n-doped Si layers[7,8], showing improved SPP confinement with respect to metal-dielectric interfaces.

Whether in microelectronics or plasmonics, the advantages of nanosecond LTA (uniform doping, high activation rate, local heating) make it a new technological advantage. If differences in thermal processing between SOI and bulk silicon have been explored, including the heat rate, dopant activation, and solid phase epitaxial regrowth in typical spike annealing or furnace annealing schemes[9–11] and more recently in the millisecond regime[12] such processes have not been extensively understood in the nanosecond regime. It is even more critical for very thin SOI layers (25 *nm* or less) and

high doping levels (up to some at. %), leading to a lack of thermal simulations for such extreme conditions. Hence, the deep understanding of the different melting regimes and regrowth processes when a thin and highly doped Si layer is submitted to nanosecond laser annealing is of outmost importance for predictive simulations and optimization of the future devices involving such processes. In this paper, a thorough study of the heavy doping of thin SOI layers is presented, involving low energy and high dose P implantation coupled to UV nanosecond LTA for efficient dopant activation. For this purpose, a panel of multi-scale characterization techniques are carried out involving in situ time resolved reflectometry, Time of Flight Secondary Ion Mass Spectroscopy, sheet resistance, Hall effect measurements coupled to atomic scale observations by advanced Transmission Electron Microscopy and Atomic Force Microscopy (AFM). The different melting regimes and further recrystallization processes involving explosive crystallization and epitaxial liquid phase epitaxy are investigated as a function of the laser energy density and doping content. The concomitant P redistribution and dopant activation processes are discussed.

II. EXPERIMENTAL DETAILS

Investigated samples are 300 *mm* Silicon-On-Insulator (SOI) substrates with thin 23±2 *nm* top silicon layer (001) and 20 *nm*-thick SiO_2 buried oxide (BOx) on top of an intrinsic Si substrate. The top silicon is implanted with phosphorus at 4 *keV* (see Fig. 1(a)). with four increasing doses (see Table I). The projected range of the implanted profiles is 7.5 *nm* with a Full Width at Half Maximum (FWHM) at 10.6 *nm* as predicted by SRIM simulations. These high dose implantations give rise to the amorphization of part of the Si top layer (see Fig. 2(a)), with depths ranging from 14.5 ± 2 *nm* for the lowest dose up to 18± 2 *nm* for the highest (Table I). The a/c interface of the remaining thin crystalline layer presents a roughness of 2 *nm*.

In a second step (Fig. 1(b)) UV nanosecond laser thermal annealing (LTA) is performed using a SCREEN-LASSE LT3100 system involving a XeCl excimer pulsed laser (λ = 308 *nm*, 4 *Hz*) with a single pulse duration of 160 *ns* and laser density energies ranging from 1.00 to 1.80 J/cm^2.

In situ time resolved reflectometry (TRR) measurements at 635 *nm* have been performed during the LTA process in order to determine the different annealing regimes. Modification in TRR signal is caused by changes in optical properties (refractive indexes) when the material temperature increases and the transition to liquid phase can be detected as the reflectivity of the liquid is much higher than the one of the solid. The signal intensity is proportional to the liquid layer thickness and intensifies as the molten layer grows until reaching a plateau which corresponds to the reflectivity in a semi-infinite liquid layer. For Si, this critical layer thickness is near 20 *nm*[13].

Specimens have been prepared in cross-section by Focus Ion Beam (FIB) for Transmission Electron Microscopy observations with a decreasing voltage from 16 *kV*-50 *pA* to 5 *kV*-15 *pA* and a last cleaning step at 2 *kV*-10 *pA* to avoid damage during the FIB preparation[14]. Structural properties were investigated by Scanning Transmission Electron Microscopy (STEM) observations using a JEOL ARM 200 F probe-corrected microscope with a cold FEG emission at 200 *kV*.

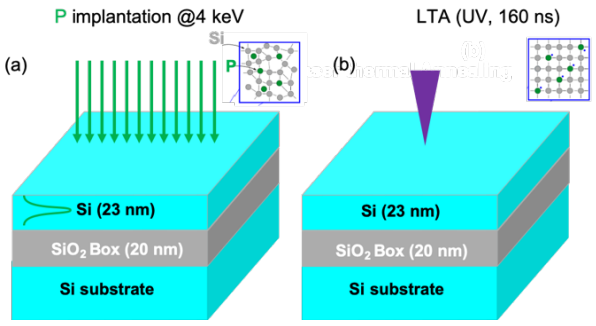

FIG. 1. Scheme describing the stack and steps for dopant introduction and activation: (a) P implantation and Si top layer partial amorphization and (b) Laser Thermal Annealing (LTA).

The surface roughness has been studied by Atomic Force Microscopy (AFM) in the tapping mode, using a Dimension D3000 AFM with a Nanoscope III controller coupled with the Basic Extender module (Bruker). Experiments were performed in clean room, with Nanosensors PPP-NCH Si tips (typical force constant: 42 N/m, tip radius of curvature < 10 *nm*.

The P implanted profiles have been measured by Time of Flight Secondary Ion Mass Spectroscopy (TOF-SIMS) in a dual beam IONTOF IV system equipped with a Cs^+ ion gun for sputtering and a Ga^+ ion gun for analysis. Measurements have been accomplished by means of Cs^+ ions at 1 *keV* and 80 *nA* and Ga^+ ions at 25 *keV* and 1 *pA*. Accurate time-to-depth conversion has been performed by measuring the average sputter velocity in a 16 *nm*-thick silicon on insulator reference samples. Calibration of the $^{31}P^-$ signals in the Si matrices was performed on the basis of experimental protocols already reported in previous publications[15,16].

Sheet resistance measurements have been performed after LTA by Four-Point-Probe for each dose and laser energy density. These measurements were performed with a WS3000 tool from NAPSON. The tips are equally distributed with 1 *mm* spacing in between, and their curvature is about 150 μm. The active carrier dose and mobility have been measured by means of Hall effect technique, using a HL5500PC Nanometrics Hall bench equipped with a 0.3 *T* magnet. Considering the extremely high active dopant concentrations expected in the investigated samples (well above $1x10^{20}$ cm^{-3}), the measured values of Hall carrier concentration and Hall mobility are corrected by using a Hall scattering factor, r_H equal to 0.9[17]. The experimental profiles measured by TOF-SIMS have been used as inputs for the Hall active dose extraction.

TABLE I. Implanted doses, concentrations at the projected range (Rp) predicted by SRIM calculations and thickness of the Si amorphized region measured by TEM.

SOI	**Q1**	**Q2**	**Q3**	**Q4**
Dose (P/cm^2)	1×10^{15}	4×10^{15}	7×10^{15}	1×10^{16}
Concentration at Rp (P/ cm^3	8.5×10^{20}	3.5×10^{21}	6×10^{21}	9×10^{21}
Concentration at Rp (at. %)	1.7	6.9	12	17
Amorphous thickness (*nm*)	14.5 ± 2	15.5 ± 2	17.5 ± 2	18 ± 2

III. RESULTS AND DISCUSSION

A. Structural evolution upon laser annealing

1. *Primary and secondary melt, explosive crystallization and liquid phase epitaxy*

The different annealing regimes and final microstructures obtained after subsequent recrystallization of the Si amorphized layer have been investigated by coupling in situ TRR measurements and TEM observations. In Fig. 2(b), the intensity of the reflectivity signal is plotted with a color map as a function of annealing time (x axis) and laser energy density (y axis) for sample Q4 (highest dose), together with the TRR profiles extracted at fixed energy densities corresponding to the different annealing regimes (Fig. 2(d), (f), (h), (j) and (l)). The associated microstructures are shown in Fig. 2(c), (e), (g), (i) and (k).

The amorphous Si (α-Si) melt and the subsequent explosive solidification are indicated by a sharp peak in the TRR color map and in the extracted profiles (Fig. 2(b) and (d)). It occurs first at 1 J/cm^2 and this is the start of the primary melt of the amorphous layer during which the so-called "explosive regime" (noted EC in the figure for explosive crystallization) occurs, when the liquid resulting from the melt of the amorphous layer solidifies at high velocities. This fast and transient process is due to the melt of the α-Si at lower temperature than c-Si[18], leading to the formation of an undercooled Si liquid layer. The latent heat released during its crystallization induces the melt of a thin layer of the underlying amorphous material. The fast solidification of this new undercooled liquid allows the crystallization process to propagate rapidly through the entire amorphized layer. Hence the regrowth of the α-Si takes place by a combination of upward and downward explosive crystallization, giving rise to a polycrystal in the entire volume of the amorphized film[19,20]. Surprisingly, the microstructure observed by TEM in Fig. 2(c) (1.1 J/cm^2) presents polycrystalline droplets extending down to 16 *nm* $\pm$ 2 *nm* (the depth of the former a/ interface) surrounded by epitaxial monocrystalline Si regions.

This phenomenon has been extensively studied for thick melt amorphous layers and different grain sizes are expected[19]: the initial liquid layer formed by the primary melt solidifies to form coarse-grained polycrystalline Si meanwhile a thin, self-propagating liquid layer travels through the remaining amorphous Si, producing fine-grained polycrystalline Si. However, in our case (i) the thickness of the whole amorphized layer is so low that a distinction between the two poly-

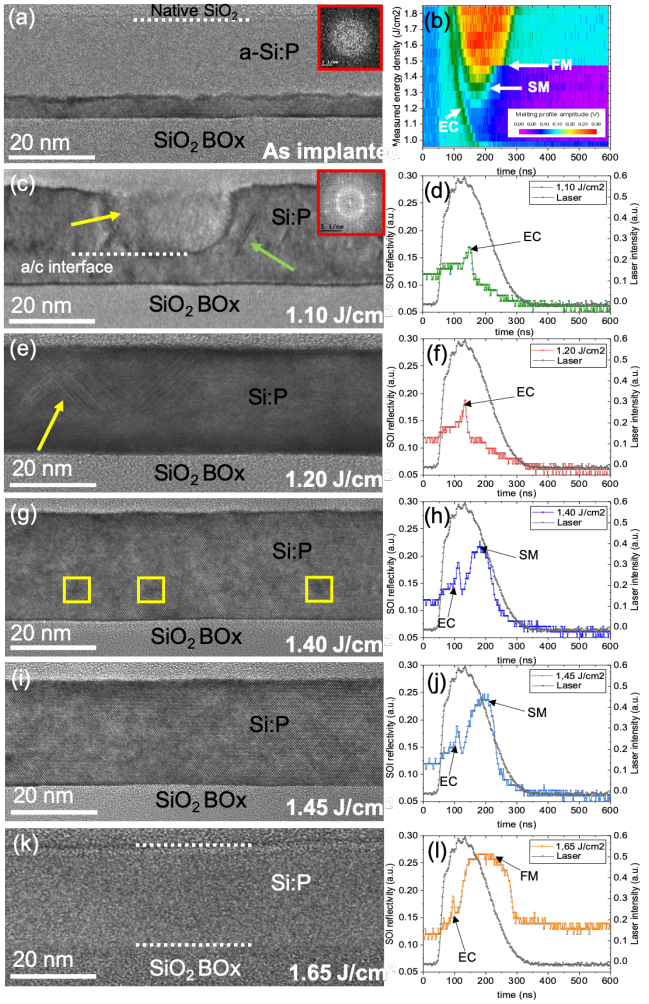

FIG. 2. (a) HREM images of the as-implanted sample; (b) TRR signal colormap: intensity of the reflectivity signal as a function of annealing time (x axis) and laser energy density (y axis) for sample Q4; (d), (f), (h), (j) and (l) are the extracted TRR profiles at energy densities of respectively 1.1 J/cm^2, 1.2 J/cm^2, 1.4 J/cm^2, 1.45 J/cm^2 and 1.65 J/cm^2. The peak with black line corresponds to the laser pulse. The different annealing regimes, namely primary melt (PM), second melt (SM) and full melt (FM) are indicated by arrows. The associated HREM images are shown in (c), (e), (g), (i) and (k).

Si layers is extremely difficult. In addition, (ii) the surface primary melt starts randomly (nucleation) as in classical phase transitions[21,22]. Indeed, for a laser pulse duration of 145 *ns*, it has been shown that melt droplets as thick as 15 *nm* can

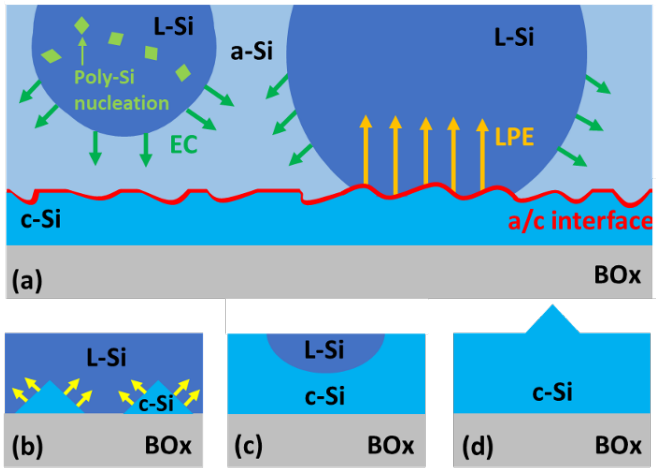

FIG. 3. (a) Comprehensive scheme for the primary melt and early solidification process of the thin amorphous Si layer by nucleation of liquid droplets at the surface with explosive crystallization (EC, green arrows) when the melt front does touch the buried c-Si layer coupled to liquid phase epitaxy (LPE, orange arrows) when the melt front reaches the crystalline seeds; (b), (c) and (d) sketch illustrating the hillock formation.

be formed (i.e. comparable to the thickness of the amorphous layers formed in this study) while adjacent areas can be melted down to a lower depth or even remain in the solid phase[23], as schematically shown in Figure 3(a). In our case, due to the difference in melting temperature between α-Si and c-Si[18], the maximum thickness of the melted droplets in the surface melt regime might well corresponds to the thickness of the entire α-Si layer (cf. large liquid droplet on the right, in Fig. 3(a). As a consequence, when the solidification of the undercooled liquid starts, the liquid droplets whose thickness is lower than the original α-Si thickness (cf. small liquid droplet on the left of Fig. 3(a)) will recrystallize according to the classical EC mechanism, resulting in a poly-Si layer (see green arrows in Fig. 3(a)). In contrast, the undercooled liquid droplets whose thickness correspond to the whole α-Si layer, will solidify epitaxially into single crystal Si from the underlying crystalline seed (orange arrows noted "LPE" for Liquid Phase Epitaxy), and grow laterally by EC (green arrows). In this case, the lateral EC proceeds with thin liquid layers which are always in contact with a single crystal so that the lateral solidification of such large droplets by EC also results in the formation of single crystal Si. This scenario is in accordance with the coexistence of polycrystalline droplets and monocrystalline Si regions observed by TEM in Fig.2 (c) (1.1 J/cm^2).

By slightly increasing the laser energy density, it is expected that the entire amorphous layer is melted during the primary melt. In such case, LPE starting from the a/c interface would occur for the whole undercooled liquid layer during solidification, and no poly-Si droplets should be formed as a result of EC. Indeed, at 1.2 J/cm^2 (see Fig. 2(e)), a monocrystalline structure is observed, together with some twin defects (indicated by yellow arrows in Fig. 2(e)), starting at a depth of 16 nm from the surface, whose formation is likely triggered by the roughness of the former a/c interface. Beyond 1.20 J/cm^2, the TRR color map with the emergence of a high reflectivity region at t=200 *ns* in Fig 2(b) suggests that, after the LPE is completed, a second melt of the solidified material occurs (labelled SM in Fig. 2). At 1.20 J/cm^2, such SM is not yet clearly detected likely because the molten thickness is still very limited. It is important to note that, unlike the primary melt, the second melt occurs at the "normal" melting temperature of silicon, leading to a more stable liquid layer.

For higher energy density (1.4 J/cm^2, Fig. 2(g)), the final regrown structure is a monocrystal with better quality compared to lower laser energies, as evidenced by the absence of twins or stacking faults. The corresponding TRR signal (Fig. 2 (h)), exhibits a more intense second melt peak, indicating a larger molten thickness. In addition, some extrinsic dislocations loops are observed, located at 21 *nm* from the surface, i.e. below the former a/c interface (cf. yellow squares in Fig.2(g)). Such defects are known to form during LTA at temperatures just below the melting point in self-interstitial rich regions[24,25]. In such conditions, some isolated and mobile liquid like droplets can be formed, that grow by a coalescence mechanism and transform into unconventional $\{001\}$ loops, as the ones observed here, through a liquid-to-solid phase transition in the nanosecond time scale. Their presence in the sample annealed at 1.4 J/cm^2 therefore reveal that the melt front did not reach the self-interstitial rich c-Si region located below the a/c interface. Indeed, a slight increase of the laser energy from 1.4 to 1.45 J/cm^2 shifts the melt front slightly deeper inside the self-interstitials rich region (as indicated by the TRR intensity increase in Fig. 2(j)) giving rise to a further improvement of the Si top layer crystalline quality, with the dissolution of the dislocation loops (cf. Fig. 2(i)).

2. *Full melt and doping effect*

For the melt/solidification regimes discussed so far (primary melt and second melt), the same recrystallization processes and final microstructures have been observed independently of the implanted doses, except for a decrease of the melt threshold when increasing the doping level (see Table SI, supplementary material). This systematic reduction of melt threshold is probably due to the lowering of the melting temperature for phosphorus-rich Si, from 1414^oC (pure Si) down to 1140^oC (SiP alloy). We cannot exclude an additional effect linked to an increase of the light absorption due to thicker amorphous layers for higher doses.

A different situation is found at higher energy densities (> 1.5 J/cm^2, for Q4) when the secondary melt front reaches the BOx interface (corresponding to the plateau observed on the TRR profiles, cf. Fig. 2(l)), i.e. when the full-melt regime is reached. Indeed, in this case the morphology of the regrown layers is strongly affected by the doping level. Hence, for samples implanted with the lowest doses (Q1 and Q2) the final structure of the Si top layer is found to be polycrystalline (see Fig. S1, supplementary material), while it is fully amorphous for the samples implanted with highest doses (Q3 and Q4) (see Fig. 2(k) for Q4). This is confirmed by the TRR

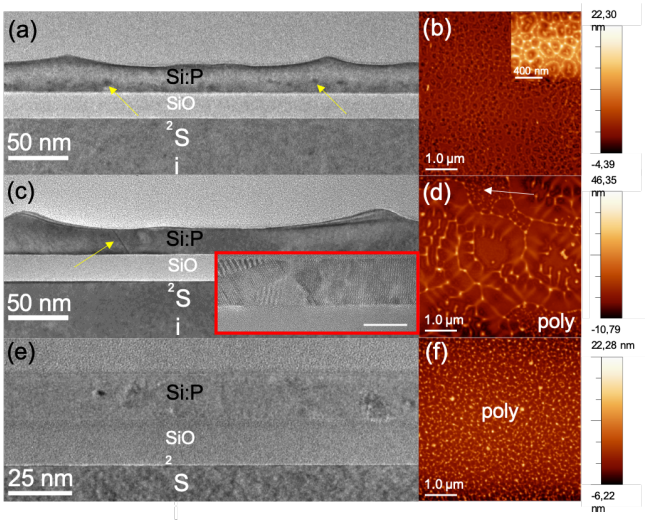

FIG. 4. (a), (c) and (e) HREM images in cross-section showing the structural morphology of the SOI layers just before (1.6 J/cm^2,) and at full melt (1.7 and 1.8 J/cm^2,) for Q1; (b), (d) and (f) associated AFM scans of the surface showing the in-plane morphology. M and P indicate respectively the monocrystalline and polycrystalline regions.

profiles at full melt which show higher baselines at the end of the anneal for Q3 and Q4 (Fig. 2(l)) compared to Q1 and Q2 (see Fig. S2, supplementary material)[26]. The polycrystalline morphology obtained after regrowth for the lower doping level (Q1 and Q2) is consistent with the estimated solidification velocity ($\leq\approx 2\ m/s$), as extracted from the negative slope of the TRR signal, for which poly-Si nucleation and growth occurs during solidification[13]. In contrast, the formation of an amorphous layer is expected for much higher solidification velocities (typically higher than 15 m/s), which have not been measured in any of the observed samples. To this respect, the formation of an amorphous layer in samples implanted with high P doses (Q3 and Q4) is then an unexpected result. A possible explanation might be based on the reduction of the crystal nucleation rate in heavily P-doped silicon, as already found in the case of solid phase epitaxy experiments[27], however further investigation are needed to confirm such hypothesis.

Finally, other structural differences can be evidenced depending on the doping level when the system approaches the full-melt regime, such as the presence of hillocks on top of the resolidified surface. For the lowest implanted dose (Q1), hillocks appear at 1.6 J/cm^2, i.e. when the secondary melt has reached the former a/c interface, as confirmed by the isolated loops indicated by yellow arrows in Fig. 4(a), whereas, the rest of the recrystallized layer is perfectly monocrystalline. The observed hillocks are about 10 nm high and 80 nm wide. Atomic Force Microscopy (AFM) scans from this sample (see Fig. 4(b)) show the random hillocks distribution on the surface plane. When increasing the energy density up to 1.7 J/cm^2, the melt front starts to overlap the interface between the Si top layer and the BOx (no loops observed in this case). At this stage, the hillocks are the most pronounced (25 nm high and 130 nm wide, see Fig. 4(c)). The layer is composed of a mix of polycrystalline and highly defective monocrystalline domains (zoom Fig. 4(c)). In the associated AFM image (Fig. 4(d)), the random network of hillocks (bright points) is clearly visible. A further increase of the energy density up to 1.8 J/cm^2 allows the melt front to fully cover the c-Si/BOx interface. A polycrystalline layer is now formed and there are no more hillocks anymore as confirmed in TEM (Fig. 4(e)). For Q2, the same type of hillocks is also observed but their domain of existence is reduced and limited to the beginning of the full melt regime at 1.55 J/cm^2 (not shown). Finally, the samples implanted with the highest P doses (Q3 and Q4) do not show any surface roughness, neither at the end of the second melt (Fig. 2(i) for Q4) nor at the beginning of the full melt (Fig. 2(k) for Q4).

The same kind of surface roughness with submicronic hillocks has been observed at the onset of the full melt regime for amorphized SOI layers[28], which was attributed to the discontinuous nature of the buried crystalline seeds remaining after the melt, and constituted by a dense array of isolated c-Si islands with the same crystalline orientation. When recrystallization occurs, these c-Si islands laterally grow leading to a network of Si hillocks at the surface.

The process of hillock generation at the surface, as a consequence of the remanence of isolated solid crystalline seeds when the melt front reaches the interface with the BOx, deserves to be deepened and a possible scenario is proposed in Fig. 3(b, c and d). The isolated crystalline seeds trigger the recrystallization of the above liquid formed during the second melt (Fig. 3(b)). When reaching the surface, these epitaxial crystalline regions let few liquid droplets, randomly distributed (Fig. 3(c)) whose solidification will give rise to surface hillocks (Fig. 3(d)). As demonstrated in Ref[22], the characteristic surface contour of the re-solidified regions at the surface is driven by faceted solid-liquid interfaces and by the difference in molar volume between solid and liquid Si, the specific volume being lower for liquid Si[29]. This surface contour presents a hillock shape, formed in the center of the transiently molten region surface, whose edge lies below the original surface level.

The formation of the hillocks at the surface is therefore conditioned by the presence of remaining isolated c-seeds after the partial melting of the buried crystalline layer up to the BOx. The remanence of such seeds is highly probable at the beginning of the full melt, when the rough melt front only partially covers the BOx interface. This process should be quenched at full melt, when the melt front is flat and totally merges the BOx interface, in good agreement with our observations.

To understand the effect of the doping of the surface hillock formation, we have to keep in mind that the thickness of the buried crystalline region decreases from 8.5 nm for the lowest dose to 5 nm to the highest one, due to the increase of the amorphization depth with the implanted dose (see Table I). As a consequence, the size of the remaining c-seeds after melt decreases when increasing the dose. This simple consideration could explain the absence of hillocks for the highest doses, as experimentally observed. Another possible explanation could

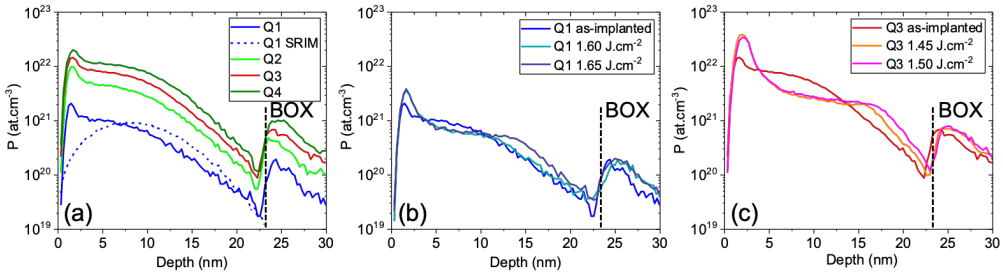

FIG. 5. : (a) ToF-SIMS measurement of the P implanted profiles for the as-implanted samples; TOF-SIMS profiles for (b) Q1 (10^{15} cm^{-2}) and (c) Q3 (7×10^{15} cm^{-2}), at the two highest laser energy densities preceding the onset of the full melt (FM).

be a reduction of the melt front roughness associated to the decrease of melt onsets with P doping as previously discussed. However, the early observation of hillocks for Q1 at the second melt remains unclear at this stage. In particular, a higher roughness of the amorphous/crystalline interface can be ruled, being the same for the different implanted doses.

Finally, whatever the implanted dose, the morphologies obtained at the onset and after full melt (polycrystalline or amorphous layer, surface hillock) do not fulfill the requirements in terms of crystalline quality for future applications, on the contrary to the monocrystalline and defect free layers obtained at the end the second melt. In the following sections, we will therefore focus only on these intermediate annealing regimes (second melt), for studying the phosphorus redistribution during the LTA process.

B. Phosphorus redistribution after LTA

The phosphorus concentration profiles were measured before and after LTA on selected samples by ToF-SIMS. Figure 5(a) shows the as-implanted profiles for all the investigated implanted doses, all exhibiting a small peak (artifact) within the first 2 *nm* below the surface. Independently of this artifact, the phosphorus concentration is highest close to the surface for all the implant doses and progressively decreases as a function of depth until the top Si/BOX interface is reached at a depth of about 23 *nm*, where a sudden increase of the ToF-SIMS signal occurs due to the substrate material change (cf. dashed line in the figure). It is important to note that the SIMS quantification procedure (and hence the corresponding concentration values indicated in the vertical axis) only applies to the top Si layer.

In all cases, the shape of the P concentration profiles slightly differs from the expected gaussian shape predicted by conventional SRIM simulations. This is probably due to the limits of such calculations that do not consider the matrix modification (P enrichment and sputtering effects) occurring during the implant, which is particularly effective for such high dose/high current processes.

ToF-SIMS phosphorus profiles were measured after LTA for all samples annealed at the two highest laser energy densities preceding the onset of the full melt (FM). For sample Q1, implanted with $1\times10^{15}cm^{-2}$ (figure 5b), these correspond to 1.60 and 1.65 J/cm^2, respectively, while for sample Q3, implanted with 7×10^{15} cm^{-2} (figure 5c), the corresponding energies were 1.45 and 1.50 J/cm^2, respectively.

Independently of the implanted dose, all the annealed samples, including samples Q2 and Q4 (not shown), show a very similar behaviour. First, a strong P pile-up is observed in the first 5 *nm* below the surface, which is followed by a quasi-plateau region with concentrations above 5×10^{20} cm^{-3} for sample Q1 (cf. Figure 5(b)), above 2×10^{21} cm^{-3} for sample Q3 (cf. Figure 5(c)) and as high as 3×10^{21} cm^{-3} or more for sample Q4 (not shown). These values largely exceed the solid solubility limit of phosphorus in bulk Si at thermal equilibrium (lower than 10^{21} cm^{-3} at the Si melting temperature)[30]. The plateau region extends to a depth corresponding to the melt depth reached during the second melt (cf. section III.A.1), which increases, as expected, when increasing the laser energy density.

The P concentration profiles measured after LTA are in agreement with those typically observed for impurities with a low partition coefficient[31]. First, during melt, due to dopant diffusivity in liquid Si being much higher than in solid Si, the implanted dopants rapidly redistribute within the liquid layer, leading to an almost perfectly flat depth profile. Then, during solidification, the phosphorus atoms are pushed into the liquid remaining layer from the solid/liquid interface, i.e. towards the surface, due to its low partition coefficient ($\approx$0.35[32,33]). This mechanism implies a continuous rejection of impurities on the liquid side of the moving interface until, when the total solidification is accomplished, a substantial fraction of the total amount of impurities is accumulated on the surface of the sample (zone refining effect). Finally, even if a strong diffusion of P toward the surface is observed after LTA, it is worth to notice that the integrated dose measured on the TOF-SIMS profiles after LTA is similar to the one of the as-implanted profiles. Hence, we can conclude that out-diffusion effects are negligible.

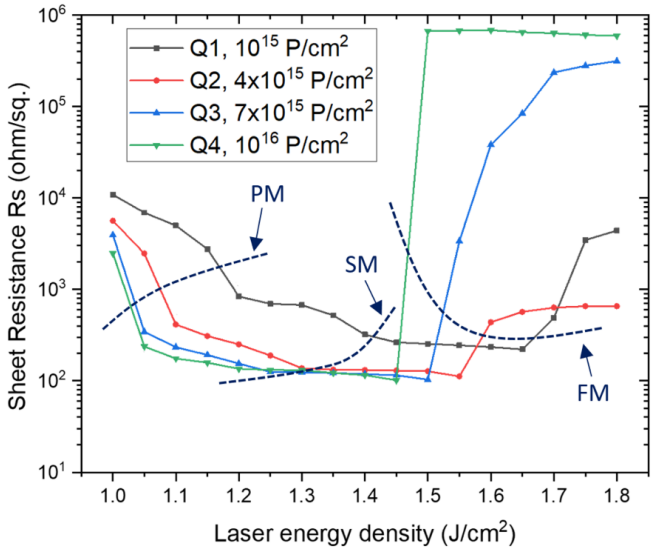

FIG. 6. Sheet resistance as a function of the laser annealing energy densities from 1.00 to 1.80 $J.cm^{-2}$ for the different implanted doses. The primary melt, second melt and full melt are indicated by respectively PM, SM and FM.

C. Phosphorus activation in thin and highly doped SOI layers after LTA

After LTA, sheet resistance measurements have been performed on all annealed samples, for laser energy densities ranging from 1.00 to 1.80 J/cm^2 as shown in Fig. 6 for the different implanted doses. Similarly to the crystal structure, the sheet resistance also evolves through different stages related to the melt/recrystallization regimes determined by the laser energy density and this, for all the implanted doses.

These different stages are qualitatively delimited by the dotted blue lines in Fig. 6. The first sudden reduction of the sheet resistance is observed in the low energy density region, in correspondence to the onset of the primary melt (cf. "PM" dotted line in Fig. 6) and the formation of the first poly-Si regions through explosive crystallization. This is followed by a slower decrease of the sheet resistance as a function of the laser energy density, presumably related to the progressive disappearance of polycrystalline regions and their replacement by defective c-Si through Liquid Phase Epitaxy (as shown for example in Fig. 2(a) for sample Q4 at an energy of 1.2 J/cm^2). This process is completed when the secondary melt is triggered (cf. "SM" dotted line in Fig. 6). In the following stage, the sheet resistance is characterized by a quasi-plateau behaviour during which the monocrystalline nature of the material mainly determines the sheet resistance value, with almost no impact from the low density of residual defects (twins, stacking faults or isolated loops). Finally, when the full melt is reached (cf. "FM" dotted line in Fig. 6), a sharp increase in the sheet resistance occurs, which is much more pronounced for the heavily doped samples (Q3 and Q4, respectively blue and green curves in Fig. 6), in agreement with their amorphous nature (cf Fig. 2(k) for sample Q4), compared to the samples implanted at lower doses, which instead exhibit a polycrystalline nature (cf Fig. S1, supplementary material).

For all melt/recrystallization regimes prior to the full melt onset, the impact of the implanted dose is clearly visible from these results. Indeed, the sheet resistance decreases when increasing the implanted dose, suggesting an increase of the active dopant density. This effect is stronger when the dose is initially increased from 1×10^{15} cm^{-2} (Q1) to 4×10^{15} cm^{-2} (Q2), then it seems to saturate when the highest doses are reached (up to 7×10^{15} cm^{-2} in samples Q3 and 1×10^{15} cm^{-2} in sample Q4), suggesting that, in the latter samples, a considerable fraction of the implanted dopants might no longer be accommodated in substitutional position.

In order to confirm this hypothesis and further investigate the dopant activation process, Hall effect measurements have been performed for all samples annealed at the three highest laser energy densities preceding the onset of the full melt (FM). The corresponding laser energy densities are respectively 0.15, 0.10 and 0.05 $J.cm^{-2}$ lower than the FM energy threshold, whose actual value depends on the phosphorus implanted dose. In the following, these laser anneal conditions will be referred to as "FM – 0.15", "FM – 0.10" and FM – 0.05", respectively. The corresponding laser energy density values are summarized in Table II.

TABLE II. Description of the 12 samples used for Hall effect analysis. For each implanted dose (samples Q1-Q4), samples annealed at the three highest laser energy densities preceding the onset of the full melt (FM) have been analyzed. The corresponding laser energy densities (in J/cm2 units) are reported in the colored cells.

	FM - 0.15	FM - 0.10	FM - 0.05
Q_1 (10^{15})	1.55	1.60	1.65
Q_2 (4×10^{15})	1.45	1.50	1.55
$Q_3(7\times10^{15})$	1.40	1.45	1.50
Q_4 (10^{16})	1.35	1.40	1.45

It is important to note that, independently of the phosphorus implanted dose, these samples exhibit the best structural and electrical properties among all the investigated ones (i.e. defect-free c-Si with minimum sheet resistance values).

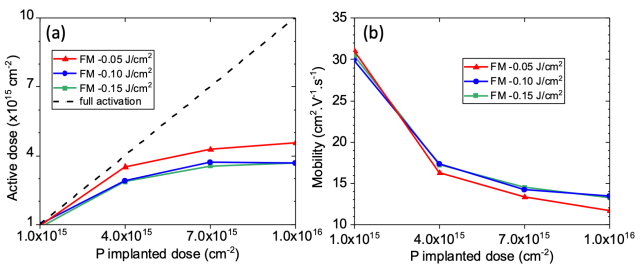

FIG. 7. (a) Hall dose and (b) mobility as a function of the phosphorus implanted dose (Q1-Q4). For each sample, the three selected laser energy densities correspond to the highest energies preceding the onset of the full melt regime.

Fig. 7 reports the measured Hall dose (Fig. 7(a)) and Hall mobilities (Fig. 7(b)), both corrected by the Hall scattering

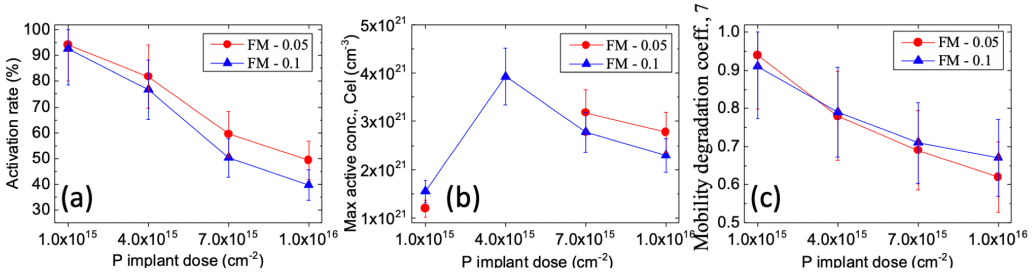

FIG. 8. (a) Activation rate, (b) maximum active concentration and (c) mobility degradation as a function of the implanted dose.

factor, r_H (cf. section II). For all annealing conditions, it is found that the Hall dose steadily increases when increasing the implanted dose. However, only for sample Q1, implanted at 1×10^{15} cm^{-2}, the Hall dose corresponds (within the experimental errors) to the implanted dose, suggesting a full dopant activation. on the contrary, for the samples implanted with the highest doses (Q3 and Q4) the measured active dose progressively saturates at values well below the total implanted dose (indicated by the dotted line in Fig. 7(a), confirming that a progressively larger fraction of the implanted dopants does not occupy substitutional positions after LTA in such samples. This behaviour is summarized in Fig. 8(a), showing the dopant activation rate estimated in samples for which a ToF-SIMS measurement of the chemical profile was performed. In parallel, and independently of the annealing conditions, the Hall mobility is found to decrease as a function of the implanted dose (cf. Fig. 7(b)). Being the carrier mobility inversely proportional to the carrier concentration, the observed mobility decrease might be simply due to the increase of the maximum active dopant concentration, Cel, when increasing the implant dose. However, a second mechanism leading to a decrease of carrier mobility might be related to the increased fraction of inactive dopants in samples implanted at high doses (cf. Fig. 8(a)). In such case, high concentrations of dopant clusters are expected to form, which may act as additional scattering centers and therefore strongly reduce the carrier mobility[34]. In any case, the mobility evolution clearly indicates that the observed decrease of the sheet resistance as a function of the implanted dose (cf. Fig. 6) is solely due to the corresponding increase of the active dopant dose.

In order to clarify the origin of the observed mobility decrease and further analyse the evolution of dopant activation as a function of the annealing conditions, raw experimental Hall effect data were analysed using the method described in Ref.[34], In practice, starting from the chemical P depth profiles measured by ToF-SIMS, the maximum active concentration, C_{el}, is first determined by fitting the measured Hall dose. The mobility degradation coefficient, α, is then adjusted in order to perfectly fit both the measured values of the Hall mobility and sheet resistance. The extracted C_{el} and α values are reported in Figs 8(b) and 8(c), respectively. For sample Q1, the results confirm that, within the experimental errors, the totality of the implanted P atoms is electrically active both at annealing conditions "FM – 0.10" and "FM – 0.05", while the measured carrier mobilities are consistent with the theoretical expected values (i.e. the mobility degradation coefficient, α, is close to unity). In contrast, for samples implanted at higher doses (Q2-Q4), the maximum active concentration, C_{el} is found to decrease when increasing the implanted dose, and this for both the "FM – 0.10" and "FM – 0.05" annealing conditions (cf. Fig. 8(b)). In addition, the mobility degradation coefficient also decreases (Fig. 8(c)) proportionally to the increase of the inactive fraction of implanted dopants in these samples. The observed decrease of the carrier mobility as a function of the implant dose (Fig. 7(b)) is therefore due to the formation of additional scattering centers related to inactive dopants, rather than to an increase of the maximum active concentration. In other words, when increasing the implanted dose, only the P atoms that penetrate deeper in the structure (cf SIMS profiles in Fig. 5(b)), are responsible for the observed increase of the active dose. In contrast, the progressive increase of the phosphorus concentration in the surface accumulation peak leads to an increased phosphorus precipitation rate, whose double consequence is (i) the decrease of the maximum active dopant concentration, C_{el}, and (ii) the increased degradation of the carrier mobility. Finally, we consider the effect of approaching the Full Melt threshold (by increasing the laser energy density) on dopant activation. For sample Q1, whose activation rate is always close to 100 %, the increase of the laser energy has little impact on both measured (Hall dose and Hall mobility, Fig 7) and extracted parameters (maximum active concentration and mobility degradation, Fig. 8). Again, a different behaviour is observed for samples implanted at higher doses (Q2-Q4). Considering for example sample Q3, implanted at a dose of 7×10^{15} cm^{-2} (a similar behaviour is observed for samples Q3 and Q4, implanted with the highest phosphorus doses), the Hall dose initially exhibits a relatively constant value ($\approx 3.6 \times 10^{15}$ cm^{-2}) for annealing conditions "FM – 0.15" and "FM – 0.10" (cf. green square and blue triangle in Fig. 7(a)), then it increases by about 20% to 4.3×10^{15} cm^{-2} for the highest laser energy density prior to full melt onset ("FM – 0.05", cf. red circle in Fig. 7(a)). This increase is accompanied by a comparatively smaller decrease (by only 9 %) of the Hall mobility from 14 to 13 $cm^2V^{-1}s^{-1}$, in agreement with the observed decrease of the sheet resistance (cf. blue triangles in Fig. 6). In addition, the C_{el} value also increases when the laser energy density in-

creases (cf. 8(b)), suggesting that the higher thermal budget associated to the increased laser energy density (both in terms of peak temperature and melt duration) favours the dissolution of phosphorus-related inactive clusters contained in the surface accumulation peak. Finally, for such optimised LTA conditions, the obtained active dopant concentrations are 2 to 4 times higher than the solid solubility of P in bulk Si at thermal equilibrium[30] at the Si melting temperature and nearly reach the highest reported active P concentration in bulk Si obtained after pulsed laser annealing, with comparable mobilities[1].

In a recent work[35], these optimised highly doped and thin layers have been successfully used as substrates for top-down processing of all-silicon-based plasmonic metasurfaces showing tuneable localised surface plasmon resonances in the IR range. Thirty years after the discovery of light emission from nano-silicon, this renewed the interest of silicon for optical applications as IR plasmonics.

IV. CONCLUSION

Hyper-doping of SOI substrates thin over-layers has been realized by coupling low energy ion implantation of P and nanosecond UV-LTA. By varying the laser energy density, the successive melting and recrystallization regimes involving explosive crystallization and classical liquid phase epitaxy have been identified. Our results highlight the complexity of such thin stratified system for which a slight shift of the spatial position of the melt front on one side and a variation of the doping level on the other side, both strongly affect the regrowth processes and final microstructures. Optimised layers with perfect crystallinity and plateau shape P redistribution have been obtained, despite the pile-up of part of the implanted P at the native oxide interface during liquid phase epitaxy. After the second melt, monocrystalline layers containing high active dopant concentrations nearly reaching the highest reported active P concentration in bulk Si are successfully reported. In addition, our dopant activation process, while reaching state-of-the-art values, does not dramatically deteriorate the electron mobility, whose decrease with the implanted dose is related to the formation of additional scattering centres related to inactive dopants rather to an increase of the maximum active concentration.

SUPPLEMENTARY MATERIAL

See the supplementary material for the table resuming the energy thresholds at the different melt regimes for increased implantation doses (Table SI) and for the microstructure at full melt (Fig. S1) and associated TRR (Fig. S2).

DATA AVAILABILITY

The data that support the findings of this study are available within the article and its supplementary material

ACKNOWLEDGMENTS

The research leading to these results has received funding from ANR DONNA (ANR-18-CE09-0034), the International Emerging Action from CNRS DONNA and EC-MUNDFAB (European Union's Horizon 2020 research and innovation program N^{o}871813) projects. SCREEN Company and its French subsidiary LASSE are gratefully acknowledged for their support in operating and maintaining the LT-3100 nanosecond laser annealing platform. We also thank the Raimond Castaing platform in Toulouse for the access to the microscopy characterization.

[1] K. Huet, F. Mazzamuto, T. Tabata, I. Toqué-Tresonne, and Y. Mori, "Doping of semiconductor devices by laser thermal annealing," Materials Science in Semiconductor Processing **62**, 92–102 (2016).

[2] M. Hackenberg, K. Huet, R. Negru, J. Venturini, G. Fisicaro, A. La Magna, and P. Pichler, "Modeling boron profiles in silicon after pulsed excimer laser annealing," Valladolid, Spain , 241–244 (2012).

[3] P. Gundel, M. C. Schubert, F. D. Heinz, R. Woehl, J. Benick, J. A. Giesecke, D. Suwito, and W. Warta, "Micro-spectroscopy on silicon wafers and solar cells," Nanoscale Research Letters **6**, 197 (2011).

[4] P. Baeri and E. Rimini, "Laser annealing of silicon," Materials Chemistry and Physics **46**, 169 (1996).

[5] F. Cristiano and A. La Magna, "Laser Annealing Processes in Semiconductor Technology: Theory, Modeling and Applications in Nanoelectronics," (2021) (elsevier, 2021) ed.

[6] S. Kerdilès, P. A. Alba, B. Mathieu, M. Veillerot, R. Kachtouli, P. Besson, H. Denis, F. Mazzamuto, I. Toqué-Trésonne, K. Huet, and C. Fenouillet-Béranger, "Dopant activation and crystal recovery in arsenic-implanted ultra-thin silicon-on-insulator structures using 308nm nanosecond laser annealing," in *2016 16th International Workshop on Junction Technology (IWJT)* (2016) pp. 72–75.

[7] J. C. Ginn, R. L. Jarecki, E. A. Shaner, and P. S. Davids, "Infrared plasmons on heavily-doped silicon," Journal of Applied Physics **110**, 043110 (2011).

[8] G. V. Naik, V. M. Shalaev, and A. Boltasseva, "Alternative Plasmonic Materials: Beyond Gold and Silver," Advanced Materials **25**, 3264–3294 (2013).

[9] A. F. Saavedra, K. S. Jones, M. E. Law, K. K. Chan, and E. C. Jones, "Electrical activation in silicon-on-insulator after low energy boron implantation," Materials Science in Semiconductor Processing **96**, 1891–1898 (2004).

[10] R. Duffy, M. J. H. Van Dal, B. J. Pawlak, M. Kaiser, R. G. R. Weemaes, B. Degroote, E. Kunnen, and E. Altamirano, "Solid phase epitaxy versus random nucleation and growth in sub-20nm wide fin field-effect transistors," Applied Physics Letters **90**, 241912 (2007).

[11] J. J. Hamilton, K. J. Kirkby, N. E. B. Cowern, E. J. H. Collart, M. Bersani, D. Giubertoni, S. Gennaro, and A. Parisini, "Boron deactivation in preamorphized silicon on insulator: Efficiency of the buried oxide as an interstitial sink," Journal of Applied Physics **91**, 092122 (2007).

[12] T. J. Michalak, J. Herman, A. Basavalingappa, M. Rodgers, D. França, and C. Borst, "Study of millisecond laser annealing on recrystallization, activation, and mobility of laser annealed SOI doped via arsenic ion implantation," Journal of Vacuum Science & Technology B, Nanotechnology and Microelectronics: Materials, Processing, Measurement, and Phenomena **33**, 011201 (2015).

[13] J. Boneberg and P. Leiderer, "On the interpretation of time-resolved surface reflectivity measurements during the laser annealing of si thin films," Physica. Status Solidi A **166**, 643 (1998).

[14] N. I. Kato, "Reducing focused ion beam damage to transmission electron microscopy samples," Journal of Electron Microscopy **53**, 451–458 (2004).

[15] M. Perego, G. Seguini, E. Arduca, J. Frascaroli, D. De Salvador, M. Mastromatteo, A. Carnera, G. Nicotra, M. Scuderi, C. Spinella, G. Impellizzeri, C. Lenardi, and E. Napolitani, "Thermodynamic stability of high phosphorus concentration in silicon nanostructures," Nanoscale **7**, 14469–14475 (2015).

[16] M. Mastromatteo, E. Arduca, E. Napolitani, G. Nicotra, D. De Salvador, L. Bacci, J. Frascaroli, G. Seguini, M. Scuderi, G. Impellizzeri, C. Spinella,

M. Perego, and A. Carnera, "Quantification of phosphorus diffusion and incorporation in silicon nanocrystals embedded in silicon oxide: Quantification of P in Si nanocrystals embedded in SiO $_2$," Surface and Interface Analysis **46**, 393–396 (2014).

[17] J. A. del Alamo and R. M. Swanson, "Measurement of Hall scattering factor in phosphorus-doped silicon," Journal of Applied Physics , 2314 (1985).

[18] F. Spaepen and D. Turnbull, "Kinetics of motion of crystal-melt interfaces," (AIP, 1979) pp. 73–83.

[19] M. O. Thompson, G. J. Galvin, J. W. Mayer, P. S. Peercy, J. M. Poate, D. C. Jacobson, A. G. Cullis, and N. G. Chew, "Melting temperature and explosive crystallization of amorphous silicon during pulsed laser irradiation," Physical Review Letters **52**, 2360–2363 (1984).

[20] S. F. Lombardo, S. Boninelli, F. Cristiano, I. Deretzis, M. G. Grimaldi, K. Huet, E. Napolitani, and A. La Magna, "Phase field model of the nanoscale evolution during the explosive crystallization phenomenon," Journal of Applied Physics **123**, 105105 (2018).

[21] J. F. Young, J. E. Sipe, and H. M. van Driel, "Laser-induced periodic surface structure. III. Fluence regimes, the role of feedback, and details of the induced topography in germanium," Physical Review B **30**, 2001–2015 (1984).

[22] K. Hennig, "Energy pulse modification of semiconductors and related materials: Part 1 and 2," (1985) akademie der wissenschaften der ddr, zentralinstitut für kernforschung rossendorf bei dresden ed., pp. 264–287.

[23] L. Dagault, S. Kerdilès, P. Acosta Alba, J.-M. Hartmann, J.-P. Barnes, P. Gergaud, E. Scheid, and F. Cristiano, "Investigation of recrystallization and stress relaxation in nanosecond laser annealed si1-xgex/si epilayers," Applied Surface Science **527**, 146752 (2020).

[24] Y. Qiu, F. Cristiano, K. Huet, F. Mazzamuto, G. Fisicaro, A. La Magna, M. Quillec, N. Cherkashin, H. Wang, S. Duguay, and D. Blavette, "Extended Defects Formation in Nanosecond Laser-Annealed Ion Implanted Silicon," Nano Letters **14**, 1769–1775 (2014).

[25] L. A. Marqués, M. Aboy, I. Santos, P. López, F. Cristiano, A. La Magna, K. Huet, T. Tabata, and L. Pelaz, "Ultrafast Generation of Unconventional { 001 } Loops in Si," Physical Review Letters **119**, 205503 (2017).

[26] D. H. Auston, J. A. Golovchenko, A. L. Simons, C. M. Surko, and T. N. C. Venkatesan, "Dynamics of Qswitched Laser Annealing,," Appl. Phys. Lett. **34**, 777 (1979).

[27] G. Olson and J. Roth, "Kinetics of solid phase crystallization in amorphous silicon," Materials Science Reports **3**, 1–77 (1988).

[28] S. Kerdilès, P. Acosta-Alba, B. Mathieu, M. Veillerot, R. Kachtouli, P. Besson, H. Denis, F. Mazzamuto, I. Toqué-Tresonne, K. Huet, and C. Fenouillet-Beranger, "Dopant activation and crystal recovery in arsenic-implanted ultra-thin silicon-on-insulator structures using 308 nm nanosecond laser annealing," in *16th Int. Workshop Junction Technol. IWJT*.

[29] V. M. Glazov and O. D. Shchelikov, "Volume changes during melting and heating of silicon and germanium melts," High Temperature **38**, 405–412 (2000).

[30] P. Pichler, "Dopants, in Intrinsic Point Defects, Impurities, and Their Diffusion in Silicon,," (2004) springer vienna ed., pp. 331–467.

[31] R. Reitano, P. M. Smith, and M. J. Aziz, "Solute trapping of group iii, iv, and v elements in silicon by an aperiodic stepwise growth mechanism,," Journal of Applied Physics **76**, 1518 (1994).

[32] H. R. Huff, T. G. Digges, and O. B. Cecil, "Hyper-doped silicon nanoantennas and metasurfaces for tunable infrared plasmonics," Journal of Applied Physics **42**, 1235–1236 (1971).

[33] S. Nakano, X. Liu, X.-F. Han, and K. Kakimoto, "Numerical Analysis of Phosphorus Concentration Distribution in a Silicon Crystal during Directional Solidification Process," Crystals **11**, 27 (2020).

[34] F. Severac, F. Cristiano, E. Bedel-Pereira, P. F. Fazzini, J. Boucher, W. Lerch, and S. Hamm, "Influence of boron-interstitials clusters on hole mobility degradation in high dose boron-implanted ultrashallow junctions," Journal of Applied Physics **107**, 123711 (2010).

[35] J.-M. Poumirol, C. Majorel, N. Chery, C. Girard, P. R. Wiecha, N. Mallet, R. Monflier, G. Larrieu, F. Cristiano, A.-S. Royet, P. A. Alba, S. Kerdiles, V. Paillard, and C. Bonafos, "Hyper-doped silicon nanoantennas and metasurfaces for tunable infrared plasmonics," ACS Photonics **8**, 1393–1399 (2021).